SAND2022-2923C

ARMA 22– 291

Thermal-Hydrological-Mechanical Characterization of the Ghareb Formation at Conditions of High-Level Nuclear Waste Disposal

Kibikas[1], W., Bauer, S. [1], and Choens, C. [1]

1 - *Sandia National Laboratories, Albuquerque, NM, USA*

Shalev, E.[2], and Lyakhovsky, V. [2]

2 - *Geological Survey Israel City, Jerusalem, Israel*

ABSTRACT: The Ghareb Formation in the Yasmin Plain of Israel is under investigation as a potential disposal rock for nuclear waste disposal. Triaxial deformation tests and hydrostatic water-permeability tests were conducted with samples of the Ghareb to assess relevant thermal, hydrological, and mechanical properties. Axial deformation tests were performed on dry and water-saturated samples at effective pressures ranging from 0.7 to 19.6 MPa and temperatures of 23 ˚C and 100 ˚C, while permeability tests were conducted at ambient temperatures and effective pressures ranging from 0.7 to 20 MPa. Strength and elastic moduli increase with increasing effective pressure for the triaxial tests. Dry room temperature tests are generally the strongest, while the samples deformed at 100 ˚C exhibit large permanent compaction even at low effective pressures. Water permeability decreases by 1-2 orders of magnitude under hydrostatic conditions while experiencing permanent volume loss of 4-5%. Permeability loss is retained after unloading, resulting from permanent compaction. A 3-D compaction model was used to demonstrate that compaction in one direction is associated with de-compaction in the orthogonal directions. The model accurately reproduces the measured axial and transverse strain components. The experimentally constrained deformational properties of the Ghareb will be used for 3-D thermal-hydrological-mechanical modelling of borehole stability.

1. INTRODUCTION

The disposal of high-level nuclear waste is a top concern worldwide (Faybishenko et al., 2017). With increasing interest in nuclear power as an alternative to carbon-based fuels, the problem of safely storing nuclear waste is expected to grow (Kim et al., 2011). One solution for disposal is geological disposal of nuclear waste, where waste is isolated within subsurface geologic formations to be contained and isolated from the surrounding environment (Birkholzer et al., 2012). Given the risks associated with nuclear waste, any potential disposal site must be demonstrably capable of isolating the material from the surface environment for large time scales (Krauskopf, 1988).

In a geological nuclear waste repository, the most important aspect of consideration is how effective the host rock will be at containing radionuclides and isolating them from groundwater. The in-situ state of stress, temperature, and hydraulic pressure in the host rock will be perturbed by construction and operation activities (Birkholzer et al., 2012). Such activities include excavation of underground openings, thermal loading generated by radioactive decay of the waste, and hydraulic pressurization generated by waste disposal. Rock mass responses to these perturbations are coupled thermal-hydrological-mechanical-chemical processes (Tsang, 1988), such that changing one condition changes the rock response to the other conditions. This response can manifest as deformation that compromise a repository's capability to isolate nuclear waste. For example, the increase in temperature from nuclear waste has been shown over time to increase horizontal stress and thus shear stress in geologic repositories of both argillitic and crystalline rock (Rutqvist, 2020). Rock damage such as fractures can provide preferential pathways for groundwater flow and radionuclide migration and represent a risk to the long-term stability of the repository. Understanding the coupled thermal-hydrological-mechanical behavior of the potential host rock is critical to evaluating its capability to isolate nuclear waste.

Many host formations worldwide have been considered for their potential as geologic repositories, though the focus has been primarily on crystalline rock, clay-rich rock, salt, and volcanic rock (Birkholzer et al., 2012). Each host rock carries with it unique challenges due to their respective geomechanical behaviors that must be accounted for during repository construction and

operation. Thus, internationally it has become standard to carefully evaluate the thermal-hydrological-mechanical processes that occur in and around a potential repository through field measurements, laboratory research, and numerical modelling to determine the potential impact of nuclear waste disposal.

In Israel, the Israeli Atomic Energy Commission (IAEC) is currently considering potential repository sites at intermediate depths for borehole disposal of nuclear waste. One potential repository is the Ghareb Formation, an organic-rich, high porosity sedimentary interval at ~500 m depth. This formation presents several unique technical challenges that must be accounted for to establish its capacity for waste disposal. The thermal-hydrological-mechanical behavior needs to be reasonably quantified and verified in a manner that allows for the prediction of any potential damage induced by installation and operation of the repository.

This work is part of a collaborative effort between Sandia National Laboratories and the Geological Survey of Israel. Expanding upon previous work (Bauer et al., 2021), a series of triaxial deformation and permeability tests were conducted with samples of the Ghareb to measure the thermal-hydrological-mechanical behavior under a variety of loading conditions and time scales. Experimental data was used to numerically model the behavior and properties of the Ghareb so the potential risk associated with borehole waste disposal can be mitigated.

2. MATERIALS AND METHODS

2.1 Ghareb Formation

The Ghareb is an Upper Cretaceous formation in Israel composed primarily of chalk, oil shales, and marl (Bisnovat et al., 2015; Shitrit et al., 2017). The target chalk unit is highly porous (Shitrit et al., 2016), possesses a high sulfur and kerogen content (Koopmans et al., 1998), and thickens to as much as 120 m in our area of study (Fig. 1).

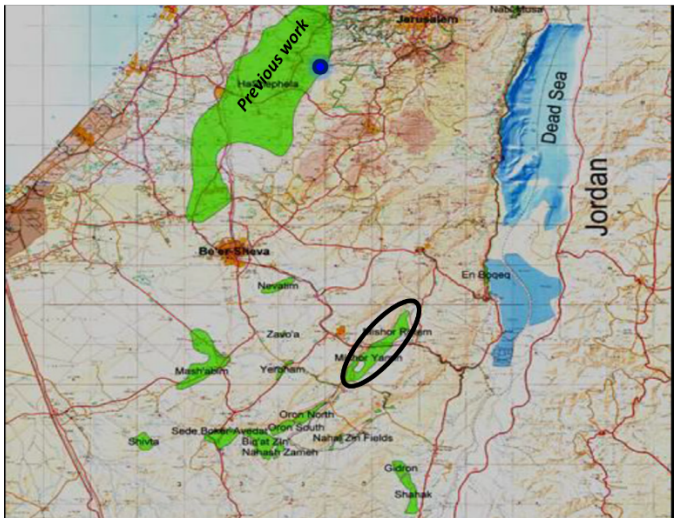

Fig. 1. Surface map of lower Israel showing previous areas of study, with the potential repository enclosed within the ellipse.

Host rock material was collected as blocks from a surface quarry (Fig. 1). The rock is massive, lacking significant bedding or obvious layering once quarried. Cored cylindrical samples were prepared into right cylinders for experimental testing according to ASTM standard (ASTM, 2010) (Fig. 2a). Each sample was oven-dried at 40 ˚C for over 24 hours before dimensions and weights were recorded prior to testing

2.2 Triaxial Tests

Samples were placed between two steel endcaps and coated with a UV cure polyurethane (Fig. 2b). Two axial and two lateral LVDTs (Linear Variable Displacement Transducers) were attached to the endcaps and across the sample diameter to measure sample deformation.

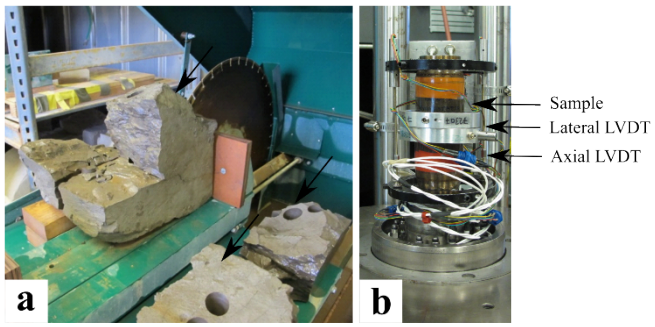

Fig. 2. a) Samples of tested material; b) sample setup for triaxial tests.

All triaxial tests were conducted using a servo-hydraulic loading (100 kN) and external pressure vessels (Fig. 3) All tests were loaded hydrostatically at a constant rate to a predetermined confining pressure (P_c) and pore pressure (P_p). Then each sample was axially loaded with a constant axial displacement rate of 10^{-5} s^{-1}. Unload-reload loops

Table 1: Testing parameters for all triaxial tests conducted.

Test Name	Condition	Temperature	P_c	P_p	Permeability
	Wet/Dry	˚C	MPa	MPa	
TP1	Dry	23	20.7	0.6	Yes
TP2	Dry	23	3.5	0.6	Yes
TP3	Dry	23	6.9	0.6	Yes
TP4	Wet	23	3.5	0.6	No
TP5	Wet	23	20.7	0.6	No
TT1	Wet	100	10.3	0.7	No
TT4	Wet	100	10.3	1	No
TT5	Wet	100	6.9	1	No
TT6	Wet	100	3.5	1	No
TT7	Wet	100	1.4	0.7	No
TT9	Wet	100	20.7	1	No

were performed during axial loading to measure the elastic moduli at various stages of deformation.

Three variations of the test procedure were used (Table 1). For the first type (TP1-TP3), dry samples were loaded to ~3.5 MPa confining pressure. Then a pore pressure was applied using gas (nitrogen) at one end of the sample with the other open to the ambient atmosphere. This created a pore pressure differential that allowed for the measurement of permeability. Samples were then allowed to sit for 1-2 days before being raised to the final confining pressure. Samples were then deformed axially with 2-4 unload-reload loops with total strains up to 9%. During each unload-reload loop, the differential stress was decreased to 0 MPa and held for ~1 hour before increasing the axial load again. Permeability was measured during these hold periods to monitor evolution with strain. Once axial loading was complete, differential stress was decreased to 0 MPa and samples were held under confining pressure for ~12-18 hours to measure the final permeability and inelastic strain. Dry tests were conducted using the 100 kN loading frame in Fig. 3a.

The second load path (tests TP4-TP5) was similar to the first type, but samples were water-saturated with similar pore pressures. Although the procedure was largely the same, with holds at confining pressure and during axial loading, pore pressure at both ends was equal to 0.69 MPa and thus permeability was not measured during hold stages. Wet tests were conducted using the 100 kN loading frame in Fig. 3a.

For the third type (TT1-TT9) of test, water-saturated samples were pressurized to the final confining pressure and a pore pressure of ~0.69 MPa. Temperature was then increased to 100 ˚C at ~1 ˚C/min and held for ~24 hours so temperature could equilibrate. Axial loading was then initiated, but during the unload-reload loops differential stress was not decreased to 0 MPa or held for any time before reloading differential stress. Wet tests at 100 ˚C were conducted using the AT 100 kN loading frame in Fig. 3b.

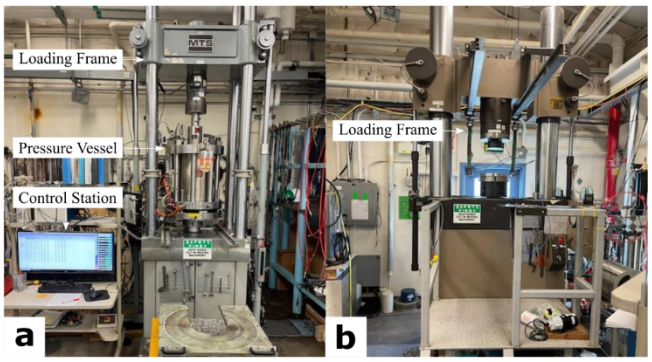

Fig. 3. a) 100 kN loading frame apparatus used for conducting room temperature tests; b) AT 100 kN loading frame used for conducting wet 100 ˚C tests.

Axial and lateral LVDTs were used to calculate the axial and radial strain (ϵ_a and ϵ_r) during testing, Volumetric strain (ϵ_v) was calculated by:

$$\varepsilon_v = \varepsilon_a + 2 * \varepsilon_r \quad (1)$$

Elastic moduli were calculated from the unloading portion of the unload-reload loop during triaxial tests. The Young's modulus (E), Poisson's ratio (ν), and shear modulus (G) were calculated from the stress and strain data using:

$$E = \frac{\sigma_{ds}}{\epsilon_a} \quad (2)$$

$$v = -\frac{\epsilon_r}{\epsilon_a} \quad (3)$$

$$G = \frac{\tau}{\gamma} \quad (4)$$

Where σ_{ds}, τ, and γ are the differential stress ($\sigma_1 - \sigma_3$), shear stress ($\sqrt{(1/3)}*\sigma_{ds}$), and shear strain ($2*(\epsilon_a - \epsilon_r)/\sqrt{(3)}$), respectively.

The apparent permeability (k) during the dry tests was determined with the formula:

$$k = \frac{2 * L * \mu * Q * (P_{dn}^2)}{A * (P_{up}^2 - P_{dn}^2)} \quad (5)$$

Where L and A are the sample length and flow cross-sectional area, respectively, P_{up} and P_{dn} are the upstream and downstream pore pressures, μ is the dynamic fluid viscosity, and Q is the volumetric fluid flow rate. No Klinkenberg correction was performed for the gas permeability calculations (e.g., Klinkenberg, 1941).

2.3 Hydrostatic Creep-Water Permeability Tests

Measurements of the long-term permeability of the Ghareb samples conducted with a customized pressure system shown in Fig. 4. Confining pressure and pore pressure were applied with three external syringe pumps (one for confining pressure, two for pore pressure).

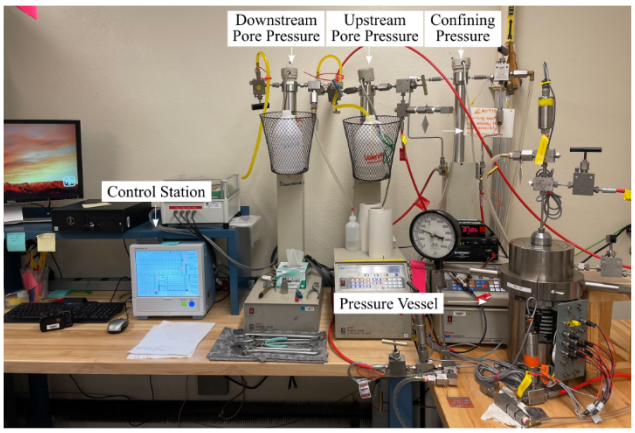

Fig. 4. The pressure vessel and setup used to conduct hydrostatic creep and permeability tests.

Samples were jacketed with LVDTs similar to the triaxial tests (Fig. 2b), then placed into a pressure vessel (Fig. 4). Confining pressure was then increased to 1-2 MPa and pore pressure both upstream and downstream to ~0.69 MPa. The samples were held at these conditions to saturate for 2-3 days. Then hydrostatic pressure was increased stepwise while upstream and downstream pressure were varied to produce a pore pressure differential. At each pressure step, conditions were maintained for several days to observe the creep and permeability (Eq. (5)), and once stable pressure was increases to the next stage. Confining pressure was increased up to 20.8 MPa, held for a period of time, then pressure was decreased in similar stepwise manner. Tests were conducted for a period of 70-100 days.

3. LAB MEASUREMENTS

3.1 Triaxial Tests

The axial and radial strain during triaxial loading of room temperature tests are shown in Fig. 5. In the range of effective pressures tested (0.7-20.3 MPa), the maximum differential stress increases with increasing effective confining pressure. In Fig. 4a, the wet tests at similar pressures exhibit much more strain per given increment of stress. The dry test samples are overall stronger, as best exemplified by the lowest pressure tests at 23 ˚C (TP2 and TP4), with dry samples exhibiting more "brittle" characteristic behavior (e.g., TP2 shows the only "drop" in stress as strain is continued).

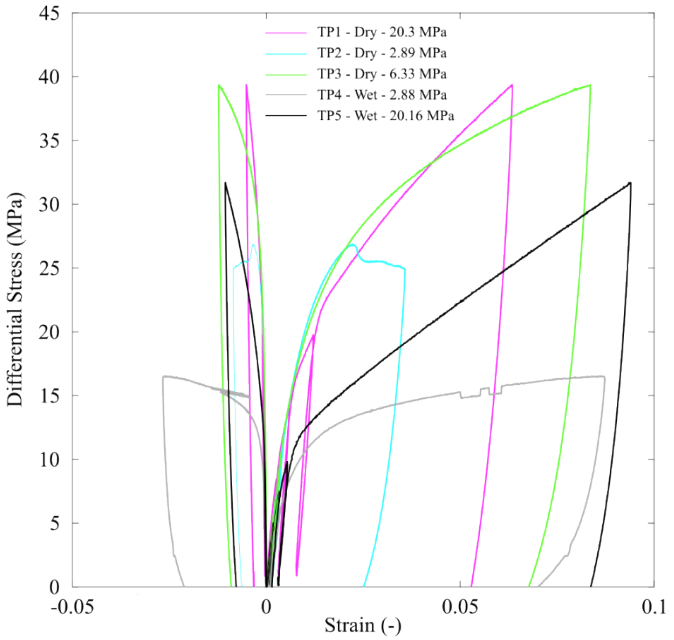

Fig. 5. Strain versus differential stress of dry and wet experiments at ambient temperatures.

By comparison, the tests at 100 ˚C are decidedly weaker than the 23 ˚C tests (Fig. 6). Differential stress in the high temperature tests is lower than what is exhibited by the tests at room temperature and similar pressure conditions.

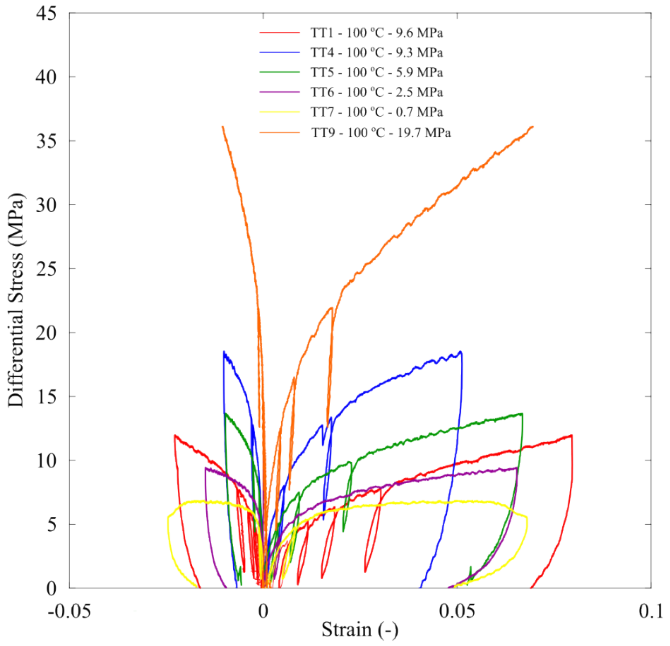

Fig. 6. Strain versus differential stress of wet experiments at 100 ˚C.

Volumetric strain continued to increase during testing at all conditions, or samples continued to compact throughout testing instead of dilating (Eq. (1)). Even at low pressure conditions (e.g., TP2, TP4, and TT7) dilatancy characteristic of significant fracturing was not observed, despite several samples post-test exhibiting localized damage along a plane.

3.2 Triaxial Permeability and Elastic Moduli

Apparent permeability measured in the dry tests (TP1-TP3) is shown in Fig. 7. Sample permeability decreases with each subsequent hold period in keeping with the increased volumetric strain. Significant permeability change is not observed between each axial loading cycle at low effective confining pressures, but TP1 shows non-negligible reduction in permeability with each subsequent application of differential stress. The permeability holds at hydrostatic conditions (Fig. 7b) show that the post-axial deformation permeability (diamonds) is significantly reduced compared to its pre-deformation hold (circles/squares) and further seems to change less as time elapses after the triaxial deformation has occurred.

The Young's modulus, Poisson's ratio, and shear modulus averaged from the unload-reload loops of each triaxial test are shown in Fig. 8. On average, the dry tests have higher Young's moduli and shear moduli than wet tests at room temperature or 100 ˚C. However. all tests seem to exhibit similar elastic moduli at the maximum effective pressure utilized (~20 MPa). The Poisson's ratio of most tests was low, on average ranging from 0.1 to 0.2. However, a higher Poisson's ratio is exhibited both at greater effective pressures and when the tests are heated to 100 ˚C (Fig. 6). The outlier of the tests was TT1, which exhibited conversely high Poisson's ratio and low Young's and shear moduli for the conditions tested.

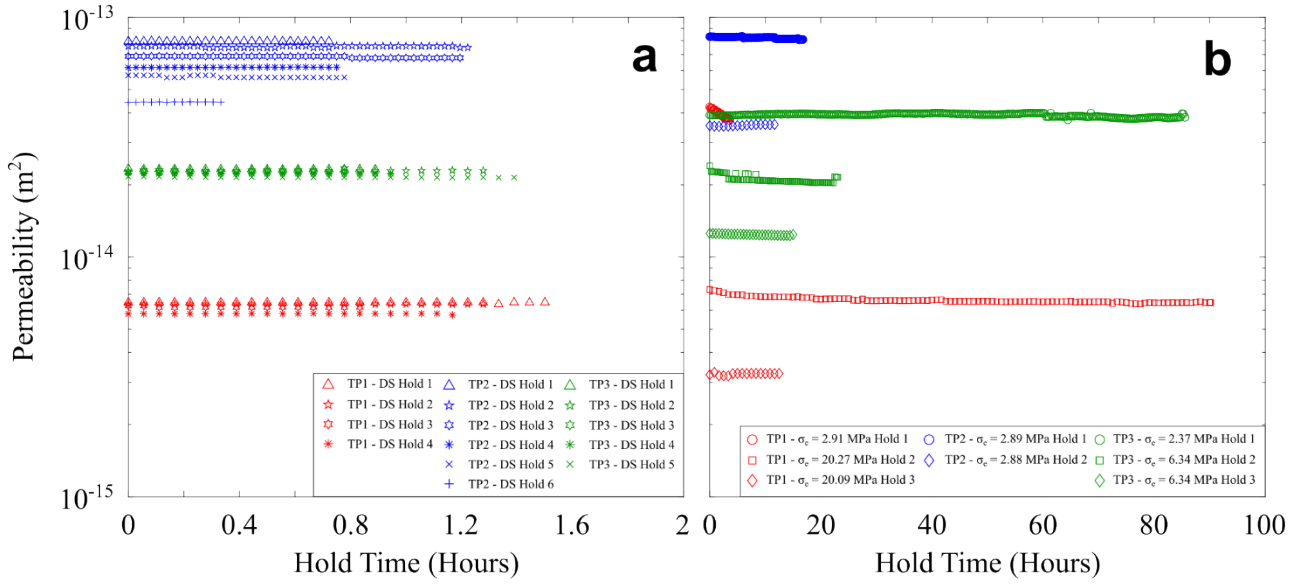

Fig. 7. a) Permeability measurements after each unload of differential stress. b) Permeability measurements pre- and post-axial loading at hydrostatic conditions; circles and square indicate pre-axial deformation measurements, while diamonds indicate post-axial deformation measurements.

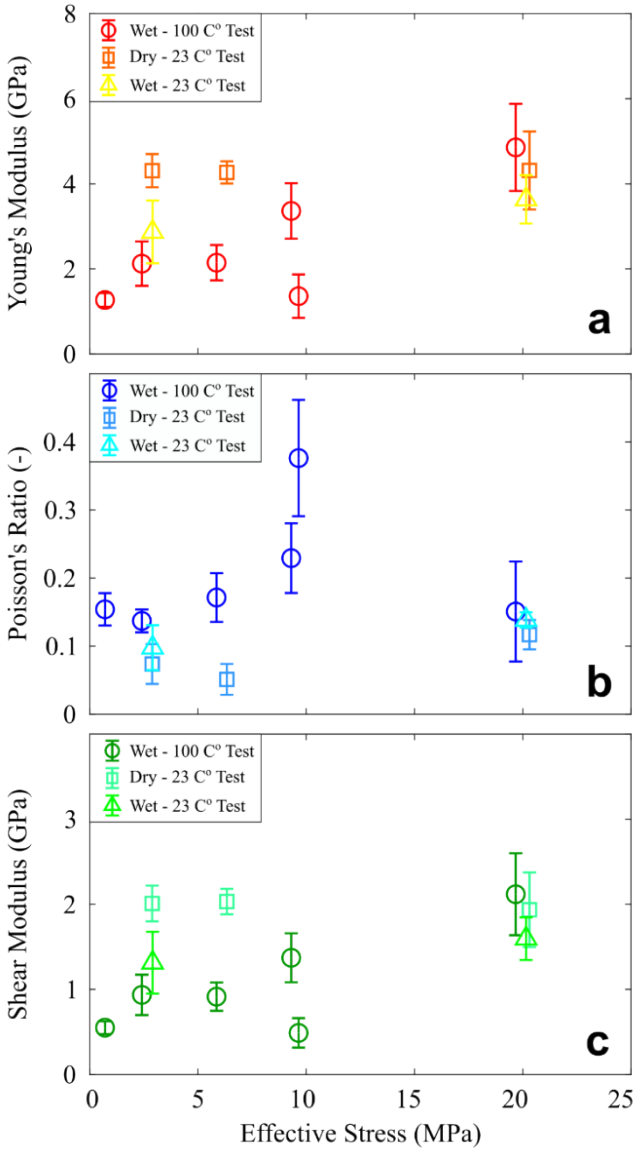

Fig. 8. Average elastic moduli calculated for the dry 23 ˚C tests (squares), wet 23 ˚C tests (triangles), and wet 100 ˚C tests (circles). a) Young's modulus; b) Poisson's ratio; c) shear modulus.

3.3 Hydrostatic Creep-Permeability Tests

Hydrostatic creep test data, including stresses, strains, permeability, is shown in Fig. 9. Both samples showed increasing strain with each increase in confining pressure and pore pressure. When pressure was held constant, strain continued to accumulate over time, with greater strain rates at greater pressures. After each decrease in pressure, strain decreased while pressure was held constant, with greater strain reduction over time at each lower pressure step.

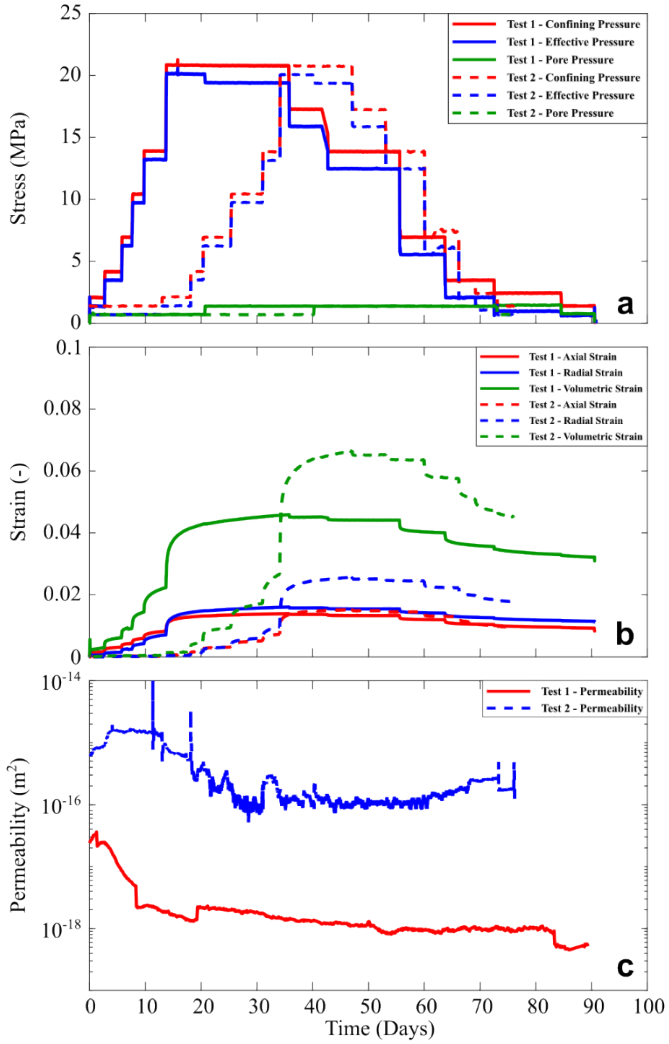

Fig. 9. Hydrostatic creep tests showing stress (a), strain (b), and permeability (c) as functions of time.

Permeability for both tests was shown to decrease by ~1 order of magnitude as effective pressure increased to 20 MPa. However, as pressure decreased, both strain and permeability remained fairly constant until effective pressure was reduced to less than 10 MPa. Test 1 did not show significant permeability increase as pressure was unloaded, due to the large amount of compaction retained (Fig 9b). Test 2 did not regain its initial permeability but did exhibit an increase in permeability when effective pressure was less than 10 MPa.

Additionally, the radial strains of both Test 1 and Test 2 became greater than the axial strains when confining pressure increased from 13.8 MPa to 20.7 MPa (Fig. 9b). Radial strain remained greater than axial strain until the test was unloaded. It should be noted that the axial strains of the two tests are similar at a given pressure condition, while the radial strain of Test 2 is nearly twice the value in Test 1 after the maximum pressurization occurs. This difference in dimension may contribute to the difference in permeability change as pressure is unloaded in the two tests (Eq. (5)).

4. NUMERICAL MODELING OF GHAREB DEFORMATION

Recently Lyakhovsky et al. (2022) discussed the directional inelastic deformation of high porosity rocks, which accumulation starts with the onset of load under room/elevated temperatures and under dry/wet conditions. To quantify this process, they define the 3-D compaction-strain tensor (Φ_{ij}). During compaction, rock volume changes, and the related volumetric strain is equal to the mean of the principal strain tensor components ((Φ_{11} + Φ_{22} + Φ_{33})/3). Isotropic compaction is often approximated empirically with Athy's law (Athy, 1930), which considers pressure-driven volumetric change and ignores shape or non-isotropic effects driven by deviatoric stress components:

$$\varphi_{eq}(P) = \varphi_f + A\exp\left(-\frac{P}{B}\right) \quad (6)$$

where $\varphi_{eq}(P)$ is the pressure-dependent equilibrium porosity achieved after long-term load under pressure P, or the mean stress equal to one-third of the stress principal values ($P = (\sigma_1 + \sigma_2 + \sigma_3)/3$); φ_f is the lowest possible porosity of the compacted rock; A and B are material properties defined from the experimentally measured and borehole-observed compaction curves. The equilibrium compaction-strain tensor connecting its value to pressure and deviatoric part of the stress tensor ($\tau_{ij} = \sigma_{ij} - P\delta_{ij}$) is (Lyakhovsky et al., 2022):

$$\Phi_{ij}^{(eq)} = A\left[\delta_{ij} - \exp\left(-\frac{P}{B_1}\delta_{ij} - \frac{\tau_{ij}}{B_2}\right)\right] \quad (7)$$

The B coefficient from Eq. (6) is replaced with two parameters, *B1* and *B2,* with units of stress.

Following compaction kinetic equations developed by McKenzie (1984, 1987), Lyakhovsky et al. (2022) suggested that the rate of the compaction process is proportional to the applied pressure times the difference between equilibrium and current compaction values:

$$\frac{d\Phi_{ij}}{dt} = C * P\left(\Phi_{ij}^{(eq)} - \Phi_{ij}\right) \quad (8)$$

where the positive kinetic coefficient, C, has units of (stress*time)$^{-1}$. This simplest extension of the existing Athy's formulation (Eq. (6)) accounts for the 3-D compaction by introducing inelastic compaction-strain tensor instead of the scalar porosity. The total strain tensor is now expressed as a sum of the elastic strain components and the compaction-strain tensor:

$$\varepsilon_{ij}^{tot} = \varepsilon_{ij}^{el} + \Phi_{ij} \quad (9)$$

This mathematical formulation is utilized here in order to reproduce the deformational processes observed in experiments on Ghareb samples under varying conditions: dry/wet saturation states, hydrostatic/triaxial stress paths, and room/elevated temperatures. Here we re-write the equations for the equilibrium compaction and its kinetics for two types of load conditions.

Under hydrostatic load:

$$\Phi^{(eq)} = A\left[1 - \exp\left(-\frac{P}{B_1}\right)\right] \quad (10)$$

This equation is equivalent to the Athy's law (Eq. 6) re-written in terms of strain or porosity change. The kinetic Eq. (8) is written for the volumetric component only:

Table 2: Parameters used for models. TT# samples were wet, TP1-TT3 were dry, and TP4-TP5 were wet.

Name	G	v	A	B_1/B_2	C_a/C_t
	MPa	-	%	MPa	%*(MPa*s)$^{-1}$
TP1	1700	0.2	20	50/40	0.0053/0.005
TP2	1700	0.2	20	50/40	0.006/0.02
TP3	1700	0.2	20	50/40	0.0048/0.01
TP4	1200	0.2	30	50/30	0.017/0.02
TP5	1000	0.2	20	50/30	0.011/0.0045
TT1	600	0.2	20	50/20	0.0057/0.008
TT4	1000	0.2	15	70/20	0.005/0.0012
TT5	800	0.2	25	50/15	0.0055/0.0015
TT6	1000	0.2	20	50/15	0.025/0.01
TT7	800	0.2	30	50/10	0.022/0.01
TT9	1000	0.2	20	50/20	0.0012/0.00035

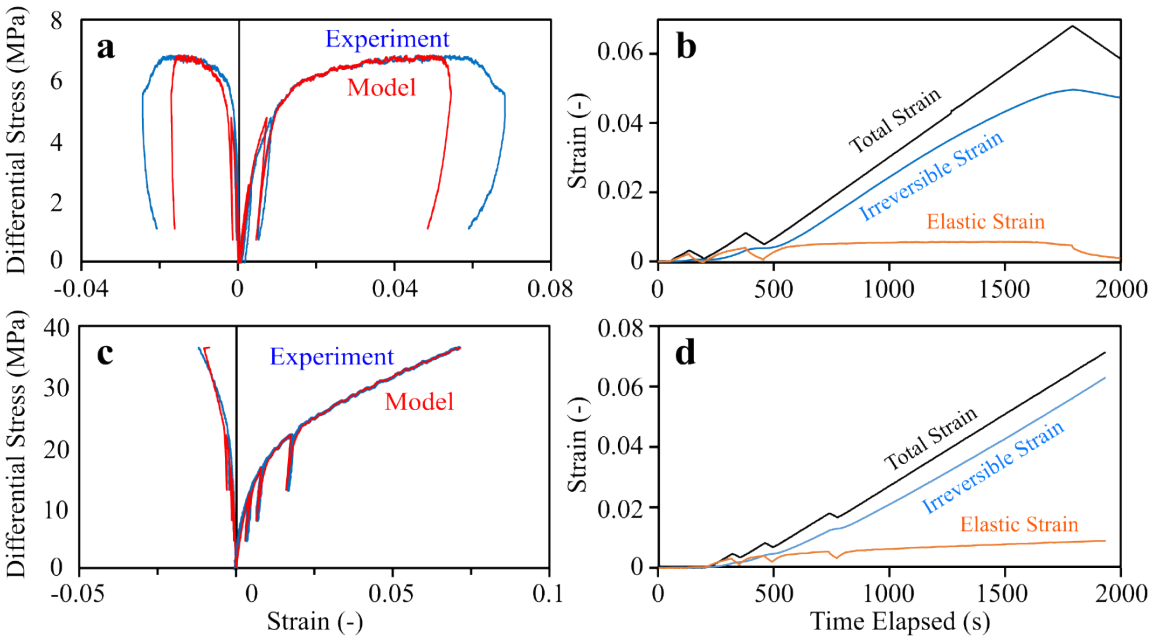

$$\frac{d\Phi}{dt} = C_h\, P\, (\Phi^{(eq)} - \Phi) \qquad (11)$$

estimated maximum compaction is almost the same for all

Fig. 10: Data and model results for triaxial experiments: a) 100 ˚C test at 0.7 MPa effective pressure showing data and model fit; b) strain components of numerical model in a; c) 100 ˚C test at 19.6 MPa effective pressure showing data and model fit; d) strain components of numerical model in c.

Under triaxial load compaction in the axial and radial directions differs and two equations for each direction are (index "*a*" for axial and "*t*" for transversal components):

$$\Phi_a^{(eq)} = A\left[1 - \exp\left(-\frac{P}{B_1} - \frac{\tau_a}{B_2}\right)\right] \qquad (12a)$$

$$\Phi_t^{(eq)} = A\left[1 - \exp\left(-\frac{P}{B_1} - \frac{\tau_b}{B_2}\right)\right] \qquad (12b)$$

and the kinetics:

$$\frac{d\Phi_a}{dt} = C_a\, P\, \left(\Phi_a^{(eq)} - \Phi_a\right) \qquad (13a)$$

$$\frac{d\Phi_t}{dt} = C_t\, P\, \left(\Phi_t^{(eq)} - \Phi_t\right) \qquad (13b)$$

Elastic moduli are calculated from the slopes of the unloading parts using Eqs. (2-4). We neglect small anisotropy and rock degradation during the experiment and calculate the elastic strain using the applied stress and constant elastic moduli. The remaining irreversible strain is modeled using Eqs. (10-13). An example for this analysis is shown in Fig. 10. We achieve a reasonable fit between measured and simulated stress-strains by choosing appropriate parameters controlling the directional compaction (Fig. 10a and 10c). Fig. 10b and 10d show that most of the observed strain is irreversible; the elastic strain components are only a small portion of the total strain. Model parameters for all experiments are given in Table 2.

The compaction-strain components in all studied samples are dominant, while the elastic strain is only small part of the observed total deformation (Fig. 10b and 10d). The

the samples (A ~ 20%) with characteristic confining pressure B_1 = 50 MPa. However, the response to differential stress significantly differs between dry and wet samples. B_2 value is ~40 MPa for the three dry samples. It is slightly lower (B_2 ~ 30 MPa) for the wet samples under room temperature and significantly lower (between 10 and 20 MPa) under 100 ˚C (Table 2). This means that enhanced compaction is expected in the Ghareb samples when water-saturated and at elevated temperature.

5. DISCUSSION

The deformation behavior of repository formations ranges from the brittle behavior of crystalline rocks to the ductile behavior of clay-rich rocks (Tsang et al., 2005; Grambow, 2016). The in-situ behavior of sedimentary rocks generally is expected to lie between these two end members – less brittle than crystalline rock but stiffer than clay-rich rocks (Perras et al., 2010).

During triaxial deformation, the samples continuously compact (i.e., positive volumetric strain) (Fig. 5, 6, 8), indicating cataclastic deformation mechanisms such as pore collapse and grain crushing outpace fracture nucleation. The relative dearth of fracture nucleation and shear failure in the triaxial tests means permeability will likely decrease gradually with continued strain rather than drop significantly as occurs after brittle failure (e.g., Bernabe et al., 2003). Fig. 9 similarly shows how permeability decreases with increased compaction (e.g.,

porosity reduction), and only partly recovers once pressure is reduced. This indicates it is unlikely the Ghareb will experience an increase in permeability due to generated stresses during repository construction and operation.

However, deformation in a repository is a coupled process, depending on more than just the mechanical load. Water-weakening is often observed in deformation of sedimentary rocks, particularly with carbonate-rich rocks like the Ghareb (Heggheim et al., 2005; Baud et al., 2009; Ciantia et al., 2015). Calcite is highly soluble compared to other rock-forming minerals; the fluid/rock interaction at the grain-grain boundary can enhance deformation of carbonate rocks through mechanisms such as stress corrosion cracking and intergranular pressure solution (Zhang et al., 2011; Ciantia et al., 2015). This appears to be occurring in our samples (Fig. 5), as the presence of water at similar effective pressures increases the strain observed for a given differential stress in the samples.

Elevated temperatures were also shown to reduce rock strength and stiffness (Fig. 6, 8), though the degree that both water and temperature alter mechanical behavior is reduced as effective pressure is increased (Fig. 8). However, the chemical-mechanical interaction over time is expected to differ due to temperature, as calcite dissolution rate increases with temperature while equilibrium concentration decreases (Plummer et al., 1978; Sjöberg and Rickard, 1984). Due to the sensitivity of calcite reactions to temperature, thermal fluctuations generated by nuclear waste disposal, along with transport properties, are expected to significantly alter both the short- and long-term deformation of the Ghareb.

The Ghareb is expected to deform mainly by compaction creep during waste disposal operations. While this can potentially reduce permeability as well given the interrelation between porosity and permeability, consistent fluid disposal may over time enhance permeability through dissolution (Bernabé et al., 2003). Numerical modelling using the experimental measurements allows for reasonable extrapolation of the deformation behavior under different thermal, chemical, hydrological, and mechanical loads. Over large time scales, these models help to mitigate the risk of compromising the geologic repository through operational activities.

6. CONCLUSIONS

This work detailed preliminary results of experimental measurement of the mechanical and petrophysical behavior of the Ghareb Formation. Triaxial test results showed the effects pressure, fluid-interaction, and temperature on deformation. Both water and elevated temperatures reduce the strength and stiffness of the samples. At higher pressures the effects of temperature and fluids on sample behavior are diminished. Permeability decreases under hydrostatic compaction creep conditions, with the rate of strain increasing at greater effective stresses.

Numerical models were formulated to evaluate and predict the strain components of the experimentally deformed samples. The model, when properly calibrated with material parameters, adequately replicates the experimental measurements, especially at higher pressures. Further modeling will be conducted to predict the permeability changes under isotropic and anisotropic stress states.

These tests and analyses, along with published literature, will be used to guide future geomechanical testing. This will allow us to better parameterize numerical simulations and establish the safety case for an intermediate depth borehole repository in the Ghareb.

ACKNOWLEDGEMENTS

Sandia National Laboratories is a multimission laboratory managed and operated by National Technology and Engineering Solutions of Sandia, LLC., a wholly owned subsidiary of Honeywell International, Inc., for the U.S. Department of Energy's National Nuclear Security Administration under contract DE-NA-0003525.

This paper describes objective technical results and analysis. Any subjective views or opinions that might be expressed in the paper do not necessarily represent the views of the U.S. Department of Energy or the United States Government. SAND2021-2484 C

REFERENCES

1. ASTM (2010). Standard test method for compressive strength and elastic moduli of intact rock core specimens under varying states of stress and temperatures. D7012
2. Athy, L. F. (1930). Density, porosity, and compaction of sedimentary rocks. *AAPG Bulletin*, *14*(1), 1-24.
3. Baud, P., Vinciguerra, S., David, C., Cavallo, A., Walker, E., & Reuschlé, T. (2009). Compaction and failure in high porosity carbonates: Mechanical data and microstructural observations. *Pure and Applied Geophysics*, *166*(5), 869-898.
4. Bauer, S., Choens, C., Kibikas, W., Shalev, E., & Lyakhovsky, V. (2021, June). Characterization and Borehole Analysis of the Ghareb Formation for Nuclear Waste Disposal. In *55th US Rock Mechanics/Geomechanics Symposium*. OnePetro.
5. Bernabé, Y., Mok, U., & Evans, B. (2003). Permeability-porosity relationships in rocks

subjected to various evolution processes. *Pure and Applied Geophysics*, *160*(5), 937-960.
6. Birkholzer, J., Houseworth, J., & Tsang, C. F. (2012). Geologic disposal of high-level radioactive waste: Status, key issues, and trends. *Annual Review of Environment and Resources*, *37*, 79-106.
7. Bisnovat, K., Hatzor, Y. H., Vinegar, H. J., Nguyen, S. V., Palchik, V., & Feinstein, S. (2015). Mechanical and petrophysical behavior of organic-rich chalk from the Judea Plains, Israel. *Marine and Petroleum Geology*, *64*, 152-164.
8. Ciantia, M. O., Castellanza, R., Crosta, G. B., & Hueckel, T. (2015). Effects of mineral suspension and dissolution on strength and compressibility of soft carbonate rocks. *Engineering Geology*, *184*, 1-18.
9. Faybishenko, B., Birkholzer, J., Sassani, D., & Swift, P. (2017). International Approaches for Nuclear Waste Disposal in Geological Formations: Geological Challenges in Radioactive Waste Isolation—Fifth Worldwide Review.
10. Grambow, B. (2016). Geological disposal of radioactive waste in clay. *Elements*, *12*(4), 239-245.
11. Heggheim, T., Madland, M. V., Risnes, R., & Austad, T. (2005). A chemical induced enhanced weakening of chalk by seawater. *Journal of Petroleum Science and Engineering*, *46*(3), 171-184.
12. Kim, J. S., Kwon, S. K., Sanchez, M., & Cho, G. C. (2011). Geological storage of high level nuclear waste. *KSCE Journal of Civil Engineering*, *15*(4), 721-737.
13. Klinkenberg, L. J. (1941, January). The permeability of porous media to liquids and gases. In *Drilling and Production Practice*. OnePetro.
14. Koopmans, M. P., Rijpstra, W. I. C., de Leeuw, J. W., Lewan, M. D., & Damsté, J. S. S. (1998). Artificial maturation of an immature sulfur-and organic matter-rich limestone from the Ghareb Formation, Jordan. *Organic Geochemistry*, *28*(7-8), 503-521.
15. Krauskopf, K. B. (1988). Geology of high-level nuclear waste disposal. *Annual Review of Earth and Planetary Sciences*, *16*(1), 173-200.
16. Lyakhovsky, V., Shalev, E., Panteleev, I., & Mubassarova, V. (2022). Compaction, strain, and stress anisotropy in porous rocks. *Geomechanics and Geophysics for Geo-Energy and Geo-Resources*, *8*(1), 1-17.
17. McKenzie, D. P. (1987). The compaction of igneous and sedimentary rocks. *Journal of the Geological Society*, *144*(2), 299-307.
18. McKenzie, D. P. (1984). The generation and compaction of partially molten rock. *Journal of Petrology*, *25*(3), 713-765.
19. Perras, M. A., Diederichs, M. S., Lam, T., Kwok, C., Armstrong, R., & Henderson, J. (2010, October). A review of excavation damage zone in sedimentary rocks with emphasis on numerical modelling for EDZ definition. In *Proceedings of the 63rd Canadian Geotechnical Conference, Calgary, Canada* (Vol. 2010, pp. 742-750).
20. Plummer, L. N., Parkhurst, D. L., & Wigley, T. M. L. (1979). Critical review of the kinetics of calcite dissolution and precipitation.
21. Rutqvist, J. (2020). Thermal management associated with geologic disposal of large spent nuclear fuel canisters in tunnels with thermally engineered backfill. *Tunnelling and Underground Space Technology*, *102*, 103454.
22. Shitrit, O., Hatzor, Y. H., Feinstein, S., Palchik, V., & Vinegar, H. J. (2016). Effect of kerogen on rock physics of immature organic-rich chalks. *Marine and Petroleum Geology*, *73*, 392-404.
23. Shitrit, O., Hatzor, Y. H., Feinstein, S., & Vinegar, H. J. (2017). Acoustic and petrophysical evolution of organic-rich chalk following maturation induced by unconfined pyrolysis. *Rock Mechanics and Rock Engineering*, *50*(12), 3273-3291.
24. Sjöberg, E. L., & Rickard, D. T. (1984). Temperature dependence of calcite dissolution kinetics between 1 and 62 C at pH 2.7 to 8.4 in aqueous solutions. *Geochimica et Cosmochimica Acta*, *48*(3), 485-493.
25. Tsang, C. F. (1988). *Coupled thermo-hydro-mechanical processes associated with a radioactive waste repository* (No. CONF-881143-). New York, NY; American Institute of Chemical Engineers.
26. Tsang, C. F., Bernier, F., & Davies, C. (2005). Geohydromechanical processes in the Excavation Damaged Zone in crystalline rock, rock salt, and indurated and plastic clays—in the context of radioactive waste disposal. *International Journal of Rock Mechanics and Mining Sciences*, *42*(1), 109-125.
27. Zhang, X., Spiers, C. J., & Peach, C. J. (2011). Effects of pore fluid flow and chemistry on compaction creep of calcite by pressure solution at 150 C. *Geofluids*, *11*(1), 108-122.